Environmental and Internal Controls on Lagrangian Transitions from Closed Cell Mesoscale Cellular Convection over Subtropical Oceans

RYAN EASTMAN,[a] ISABEL L. MCCOY,[b,c] AND ROBERT WOOD[a]

[a] *Department of Atmospheric Sciences, University of Washington, Seattle, Washington*
[b] *University Corporation for Atmospheric Research, Boulder, Colorado*
[c] *Rosenstiel School of Marine and Atmospheric Science, University of Miami, Miami, Florida*

(Manuscript received 10 September 2020, in final form 29 April 2021)

ABSTRACT: Classifications of mesoscale cellular convection (MCC) for marine boundary layer clouds are produced using a supervised neural network algorithm applied to MODIS daytime liquid water path data. The classifier, used in prior studies, distinguishes closed, open, and cellular but disorganized MCC. This work uses trajectories in four eastern subtropical ocean basins to compare meteorological variables and the structures of boundary layers for trajectories that begin as closed cells but evolve into either open cells or disorganized cells or remain closed cells over one afternoon–afternoon cycle. Results show contrasts between the trajectory sets: Trajectories for MCC that remain closed cells are more frequently observed nearer coasts, whereas trajectories that break into open and disorganized cells begin farther offshore. The frequency at which closed cells transition to open cells is seasonally invariant. The fraction of trajectories that stay as closed MCC varies throughout the year in opposition to those that break into disorganized cells, so that their annual cycles are 180° out of phase. Trajectories remain as closed cell more frequently in austral spring and boreal summer when the trade inversion is stronger. The closed–disorganized MCC breakup is associated with weaker subsidence, a weaker inversion, a drier free troposphere, and enhanced nighttime boundary layer deepening, consistent with a warming–drying mechanism. The closed–open transition occurs in meteorological conditions similar to closed–closed trajectories. However, prior to the transition, the closed–open trajectories exhibit stronger surface winds and lower cloud droplet concentrations and rain more heavily overnight. Results suggest that multiple, independent mechanisms drive changes in cloud amount and morphology.

KEYWORDS: Atmosphere; Subtropics; Clouds; Stratiform clouds; Classification

1. Introduction and motivation

Low-altitude, optically thick marine clouds cool Earth's oceans by reflecting sunlight and emitting infrared radiation to space (Hartmann et al. 1992; L'Ecuyer et al. 2019). Marine low clouds cover nearly 200 million square kilometers of ocean on average during the day (Hahn and Warren 2007), while overcast marine cloud scenes are estimated to reflect 30%–40% (Bender et al. 2016) of incoming solar radiation. Taken together, the extent and albedo of marine clouds has an effect equivalent to covering 60–80 million km^2 of dark ocean with reflectors that scatter 100% of incoming radiation back out of the atmosphere. Variations in marine cloud brightness and cover can therefore have significant consequences for climate.

Attempts to understand the mechanics of marine cloud cover evolution have been made using a variety of approaches: Comparing long-term climatologies (yearly, seasonal, and monthly) of cloud cover and environmental predictor variables shows correlations between variables (e.g., Norris 1998), although no single variable predicts a majority of cloud variability on subseasonal time scales (Klein 1997). Further, relationships between variables are difficult to disentangle and causality cannot be attributed to predictors without a time dimension (Qu et al. 2015; Klein et al. 2017). In situ studies using aircraft or ships can collect a large amount of data at a very high resolution, but they lack the longevity needed to build up statistical significance and typically lack the spatial extent needed to follow cloud scenes as they respond to their environment while advecting downstream. Studies using computer models capable of resolving circulations on the subcloud level can isolate predictors and assess causality, but they are computationally expensive and exist at the mercy of parameterized model physics (Guichard and Couvreux 2017). Here we use a newer Lagrangian approach (introduced in Eastman and Wood 2016): Following thousands of cloudy parcels as they evolve in time and space while sampling cloud properties and environmental drivers twice daily using sun-synchronous polar-orbiting satellites and reanalysis grids. This approach provides sample sizes large enough to attain statistical significance and control for confounding behaviors, while also assessing precursors to cloud changes with the introduction of a time dimension.

This work is concerned with the Lagrangian evolution of the cellular organization of stratiform clouds over the subtropical oceans (Agee 1987). In marine environments characterized by a strong temperature and humidity inversion (as is often observed in the eastern subtropical oceans), a cool and moist boundary layer is typically observed under a warm and dry free troposphere. Here stratocumulus (Sc) clouds tend to organize into broad, overcast, optically thick closed mesoscale cellular convective (MCC) clouds, whose cells are sustained by overturning driven by radiative cooling at cloud top (Wood 2012). Occasionally closed MCC clouds break into open MCC clouds, which are characterized by relatively narrow bands of optically thick clouds flanked by optically thin "veil clouds"

Corresponding author: Ryan Eastman, rmeast@atmos.washington.edu

DOI: 10.1175/JAS-D-20-0277.1

(Wood et al. 2018) with broad clear regions between the cloudy edges (Wood et al. 2008). As they advect equatorward and westward in the trade winds, subtropical closed and open cells eventually evolve into less tightly organized, more cumuliform structures (Muhlbauer et al. 2014) with sparsely distributed cloudy cells, sometimes surrounded by thin veil clouds and fields of shallow cumulus. These tropical trade wind cloud fields also frequently organize into distinct, quantifiable structures (Stevens et al. 2020), although for the purposes of this study they will be characterized as ''cellular but disorganized'' (shortened to ''disorganized'' here), since they lack the distinct repeating structures seen in closed and open MCC Sc clouds.

The drivers of transitions from closed to open cells versus closed to disorganized cells are the focus of this work. Prior research suggests that open cell formation from existing closed cells is triggered by precipitation processes (Wang and Feingold 2009). Savic-Jovcic and Stevens (2008) use a large-eddy simulation to show how cool and moist perturbations in near-surface airmasses formed by evaporation of rain drops (cold pools) can shape and propagate convective elements in drizzling Sc. Terai and Wood (2013) state that cold pool processes do exert thermodynamic and dynamic forces on the planetary boundary layer (PBL), but they stop short of showing that they are responsible for any changes in cellular organization. Precipitation was tested as a possible driver of subtropical Sc breakup in Eastman and Wood (2016) but was found to be of little importance after controlling for the depth of the boundary layer, which covaries positively with rain rate. Instead, processes that warm and deepen the boundary layer appeared more important for Sc breakup. However, that work did not assess changes in cellular structure, and it is possible that evolution from closed to open cells is associated with different processes than the evolution from closed to disorganized cells.

The Lagrangian evolution of overcast Sc clouds has recently been shown to be sensitive to the cloud droplet number concentration N_d and effective radius of cloud drops, which vary in opposition to one another (Abel et al. 2020; Christensen et al. 2020). Christensen et al. (2020) used a Lagrangian framework with geostationary satellite data in the Southeast (SE) Atlantic Ocean to show that overcast Sc cloud decks are longer lived in stable marine conditions when N_d is higher. A Lagrangian study farther offshore in the SE Atlantic done by Abel et al. (2020) used aircraft and geostationary satellite data to show that cloud drops were significantly larger (and therefore fewer in number) in a pocket of open cells (POC) relative to surrounding close cells. Their Lagrangian analysis compares 24-h back trajectories initialized within and outside the POC, showing equivalent effective radii, cloud amount, and above-cloud aerosol concentrations 24-h before breakup. Abel et al. (2020) goes on to show that the open cells studied entrain less free-tropospheric air downward into the boundary layer relative to neighboring closed cells that sit beneath a uniformly polluted troposphere. These recent results show that microphysical processes can affect cloud evolution, and that cellular structure has a significant effect on entrainment processes.

The cellular structure of marine clouds affects albedo in a few ways: Closed cells are typically cloudier than open, which are in turn cloudier than disorganized cells. Further complicating the picture, closed cells have been shown to have a higher albedo for an equivalent cloud amount versus open (I. L. McCoy et al. 2017), and disorganized cells (I. L. McCoy et al. 2017, personal communication) indicating that cloud condensate and microphysical properties are also likely important for setting scene albedo in addition to cloud cover. Watson-Parris et al. (2021) shows that the existence of pockets of open cells within broader closed cell Sc does lead to an increase in solar radiation received at the surface, though the radiative effect is small when only considering pockets of open cells. This necessitates further study of these organizational structures to understand what meteorological conditions and internal processes may be driving transitions in cellular organization. Climate models that use parameterizations based on meteorological conditions and thermodynamic structure to simulate cloud properties will be improved if they can better simulate cloud cellular properties and the conditions associated with them.

Cellular structures in clouds can now be detected and defined using high-resolution satellite imagery and efficient machine-learning techniques (Wood and Hartmann 2006; Stevens et al. 2020; Yuan et al. 2020; Denby 2020). Identifications from the supervised neural network algorithm developed in Wood and Hartmann (2006) are combined with our aforementioned Lagrangian analysis to study the evolution of cloud structures as they advect in the subtropical trade winds, identifying key precursors of changes in cellular organization. The details of this methods are presented in section 2. In section 3, we examine the meteorological conditions and internal cloud processes associated with MCC evolution. In section 4, we contrast our results with prior work, in which MCC classifications were not identified, in an effort to more accurately represent distinct cloud processes.

2. Methods and data sources

a. *MCC classifier*

The cellular organization of marine cloud cover is determined using a supervised neural network algorithm developed in Wood and Hartmann (2006). The three-layer back propagation neural network is used to classify $256 \times 256\ \text{km}^2$ scenes of Moderate Resolution Imaging Spectroradiometer (MODIS) daytime only liquid water path (LWP) (King et al. 2003) into one of three cloud types: ''closed cells,'' ''open cells,'' and ''cellular but disorganized.'' In this study, these titles are shortened to ''closed,'' ''open,'' and ''disorganized,'' respectively. A fourth classification category in the original algorithm for ''homogeneous/no organization'' has been collapsed into the closed cells type because of its limited occurrence, as in Muhlbauer et al. (2014) and I. L. McCoy et al. (2017).

Two sources of information from each scene are used as inputs to the neural network: (i) the LWP probability density function, and (ii) the LWP power spectrum from a spatial fast

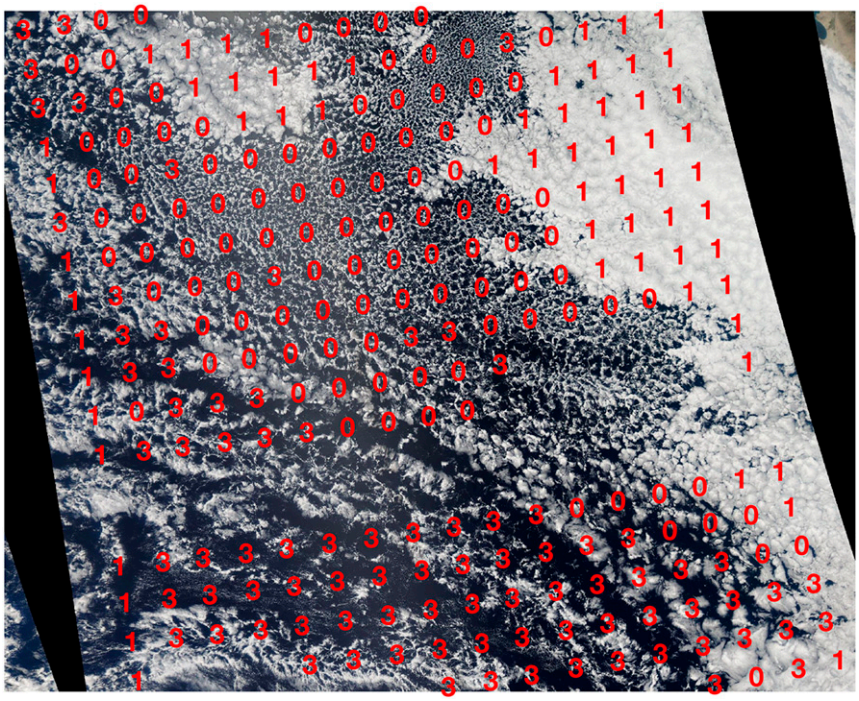

FIG. 1. Mesoscale cellular convection classifications overlaid on the corresponding MODIS *Aqua* image of clouds in the SE Pacific on 28 Sep 2007. Classifiers are defined as 0—open cells, 1—closed cells, and 3—disorganized cells. Trajectories only originate from areas where the majority of cells are labeled as "1."

Fourier transform. This ensures that the neural network is trained to classify cloud morphologies by considering both the quantity of liquid water in the scene and its spatial arrangement (i.e., level of cloud clustering), emphasizing the distinctions in cloud micro- and macrophysics between morphologies in addition to their cloud coverage. One thousand cloud scenes were hand identified by cloud type and used to train the neural network until an 85%–90% accuracy rate was reached when tested (Wood and Hartmann 2006). Scenes with overlying mid- to high-altitude clouds are removed from the dataset when the difference between cloud-top temperature and sea surface temperature exceeds 30°C (I. L. McCoy et al. 2017). Centers of classified scenes are spaced 128 km apart, producing overlap between each classified box and increasing the number of scenes that can be classified from each MODIS swath.

Previously, this neural network has been applied to single years of MODIS *Terra* collection 4 (Wood and Hartmann 2006) and *Aqua* collection 5.1 (Muhlbauer et al. 2014; D. T. McCoy et al. 2017). Here, this algorithm is newly applied to MODIS *Aqua* collection 6.1 for multiple years 2007–10. An example of the classifier is shown in Fig. 1, where classifier output is overlaid on a MODIS *Aqua* daytime cloud scene. Numbers represent MCC classifications, where 0 is open cells, 1 is closed cells, and 3 is disorganized.

Figure 1 shows a few MCC classifications that appear incorrect. In particular, there are a number of cells misclassified as "1" on the western edge of the swath that are clearly open or disorganized scenes. To evaluate whether the classifier produces results reliable enough for study, we have visually inspected the MCC classifications on 20 images, 10 in the Northeast (NE) Pacific Ocean and 10 in the Southeast (SE) Pacific in June and October, respectively. This includes a total of 3878 classifications in boxes spanning 10° latitude and 25° longitude. A visual assessment counting classifications that could be considered "unambiguously wrong," meaning another classification is clearly correct to an observer (the first author, who had no part in developing the algorithm), shows that open cells are misclassified ~16% of the time, closed cells are misclassified ~12% of the time, and disorganized but cellular scenes are misclassified ~7% of the time that they are observed. While we would prefer these numbers to be 0%, this lends legitimacy to the classification analysis, since the vast majority of scenes classified as an MCC type are actually that type, at least ~84% of the time. This is consistent with the 85%–90% accuracy rate of the neural network algorithm when it was originally developed and tested.

To determine an MCC classification for scenes observed and tracked in our Lagrangian system, a frequency distribution of all MCC box centers within 200 km of each Lagrangian sampling point is produced at each point. If any MCC classification occurs more than 50% of the time in the scene distribution, that scene is considered to be the dominant MCC type. This analysis was repeated using two other approaches for classifying scenes, producing qualitatively identical results: 1) assign the single MCC classification nearest to the trajectory sample as

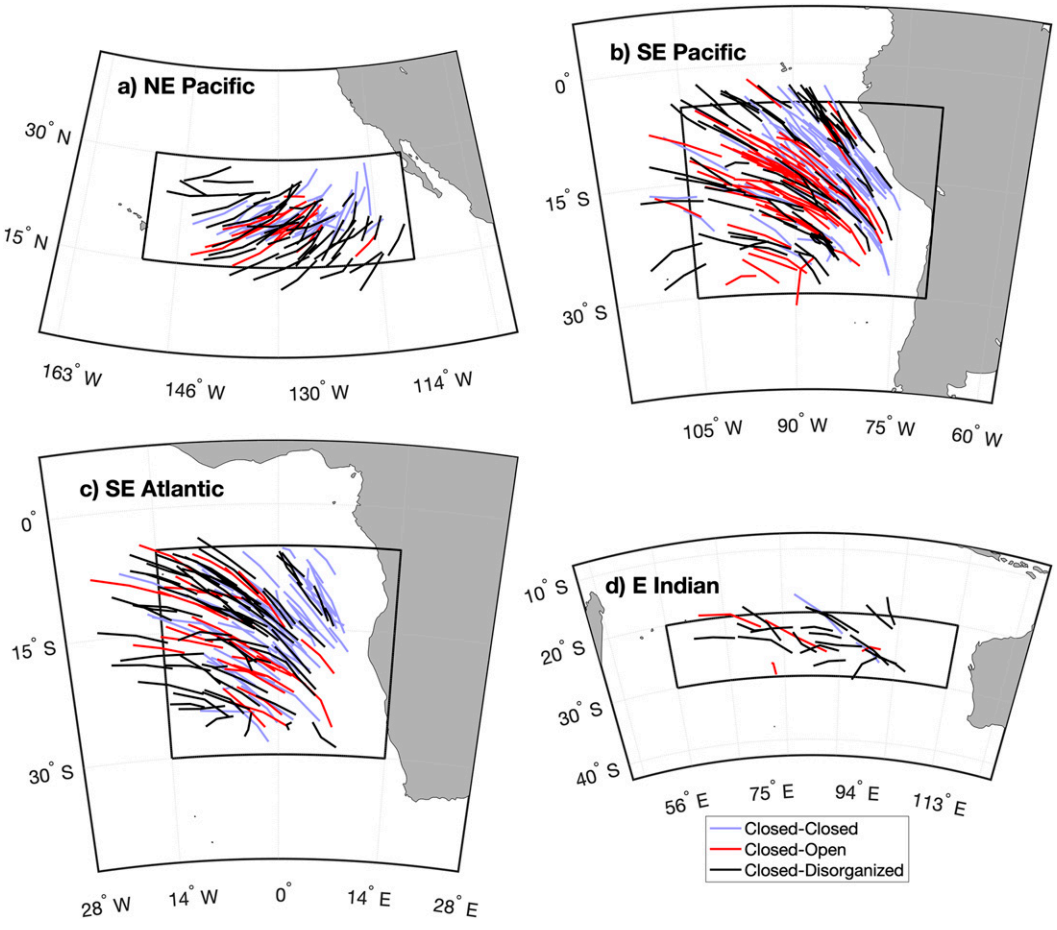

FIG. 2. Examples of 24-h trajectories used in this study (1 in 20 are shown) in our four study regions: (a) NE Pacific, (b) SE Pacific, (c) SE Atlantic, and (d) E Indian. All trajectories begin as closed. Blue trajectories remain closed, red trajectories transition to open cells, and black trajectories transition to cellular but disorganized cells after 24 h.

the MCC type for that sample and 2) assign the sample MCC type to the majority MCC type in the frequency distribution, not requiring 50% or greater representation.

b. *Lagrangian framework*

Trajectories used in this Lagrangian study are identical to those used in Eastman et al. (2017) and Eastman and Wood (2018). They are generated from isobaric ERA-Interim (Dee et al. 2011) wind fields at 925 hPa using the routine introduced in Bretherton et al. (2010). Trajectories are initiated along the *CloudSat*/*Cloud–Aerosol Lidar and Infrared Pathfinder Satellite Observations* (*CALIPSO*) curtain, spaced 200 km apart in four subtropical ocean study regions, shown in Fig. 2 and defined below, for years 2007–10. To capture two diurnal cycles while advecting westward in the trade winds, trajectories are run for 54 h. This extra time is necessary given that the westward advection of trajectories follows the arc of the sun overhead, slightly lengthening the time between sunrises. In total, ~170 000 54-h trajectories are used. Samples of cloud and meteorological data are taken concurrent with each Afternoon-Train (A-Train) flyover at times defined as $T = 0$, 12, 24, 36, and 48 trajectory hours. Note, however, that the timing in UTC hours between each sample time is, on average, slightly longer than 12 h because of the westward advection. Sample points include all data within a 100-km radius of each observation point. A 100-km radius is chosen in order for each sample to contain several 1° × 1° latitude/longitude L3 grid boxes so as to generate robust averages. Different sample radii were investigated in Eastman et al. (2016), which showed that Lagrangian tendencies were consistent between 100-km radii and larger radii up to 1200 km.

Here, we focus on 24-h (1330–1330 LT) Lagrangian transitions in MCC classifications, specifically looking at trajectories that begin as closed cell Sc. Our 54-h trajectories are split into 24-h segments. Each segment contains one day-to-day diurnal cycle. This segmenting is done by splitting 54-h trajectories that begin during the day into two segments: one that spans 0–24 h, and another that spans 24–48 h. For trajectories initialized at night, only the span from 12 to 36 h is used. This creates just over 250 000 24-h trajectory segments.

Trajectory segments, also called ''trajectories,'' are composited into three sets based on their 0-h and 24-h MCC classifications: closed–closed, closed–open, and closed–disorganized. Requiring our trajectories to all begin as closed cells allows for a greater ''apples to apples'' comparison since retrieved cloud variables at 0-h may otherwise be artificially affected by different cellular structures. The afternoon–afternoon time period is constrained by the MCC data, which are only collected during the daytime overpass of the *Aqua* satellite at 1330 local time. Given this constraint, there is no bias in our results due to compositing of nonmatching diurnal cycles. Nighttime data are collected concurrent with the 0130 local-time overpass of the *Aqua* satellite. Plots of these trajectories, colored based on transition type, are shown in Fig. 2, which also highlights the geographic bounds of our study regions.

Study regions are chosen in four eastern subtropical ocean basins with similar climatologies, chosen to capture Sc maxima near the west coasts of major continents and also the declining cloud cover gradients farther offshore as the Sc transition into trade cumulus (Cu). These regions are identical to those in Eastman and Wood (2016, their Fig. 1), and are named the Northeast Pacific, Southeast Pacific, Southeast Atlantic, and the East (E) Indian regions. These regions are also illustrated here in the maps in Fig. 2. The E Indian region was chosen instead of the also-relevant Northeast (NE) Atlantic after an analysis of trajectories showed a greater amount of synoptic influence in the NE Atlantic, characterized by a significant fraction of trajectories abruptly changing direction from westward to eastward. This synoptic behavior, which can interfere with the cloud processes we hope to study here, was less frequent in the E Indian Ocean.

c. *Cloud and meteorological data*

This work will combine several data sources from polar orbiting satellites and model reanalysis fields. Satellite data come from several platforms orbiting in NASA's A-Train constellation, including MODIS and the Advanced Microwave Scanning Radiometer for EOS (AMSR-E) both orbiting aboard the *Aqua* satellite, the *CALIPSO*, and the spaceborne cloud profiling radar aboard *CloudSat*. The A-Train satellites orbit together with equator crossing times at 0130 and 1330 local times, allowing for near-simultaneous sampling of atmospheric features by several different instruments. Meteorological data come from the ERA5 reanalysis (Copernicus Climate Change Service 2017). Reanalysis data fields are interpolated to match the observation times of the A-Train satellites. ERA5 meteorological variables used in this study are Surface wind speed, subsidence at 700 hPa ω_{700}, sea surface temperature (SST), lower-tropospheric stability (LTS; θ_{700}–θ_{1000}), and humidity at 700 hPa q_{700}. These variables are referred to as ''environmental'' or ''meteorological'' variables and are tested as drivers of MCC evolution. Lower-tropospheric stability is chosen as our measure of inversion strength instead of estimated inversion strength (EIS) due to the strong correlation between EIS and q_{700}, which is shown to be a strong cloud controlling variable in the Lagrangian realm (Eastman and Wood 2018). The use of LTS in lieu of EIS should not negatively impact results, since this study takes place exclusively within the subtropics (Wood and Bretherton 2004).

Cloud cover data retrieved along trajectories for day and night come from the mean cloud fraction values in the MODIS cloud mask dataset (Hubanks et al. 2008; Oreopoulos 2005). These are available twice daily on the uniform 1° × 1° latitude/longitude (L3) grid. The MODIS swath is over 2000 km wide, requiring sensor viewing angles over 60° from nadir at the swath edge. Geometric issues arise when clouds are viewed from this oblique angle, causing a high bias in cloud amount at swath edge (Maddux et al. 2010). This Lagrangian project uses MODIS retrievals taken along trajectories that originate on the *CloudSat*/*CALIPSO* curtain at hour 0 for every 54-h trajectory. This means that the sensor zenith at trajectory outset is always around 19° but is usually wider at subsequent observation times. Because cloud amount is biased higher at wider angles, a correction is necessary to avoid a spurious increasing tendency in cloud amount driven by the changing view angle. This zenith angle bias is accounted for by subtracting the mean excess in cloud cover from each sample caused by that sample's view angle (Eastman and Wood 2016), which can be as high as 14% at swath edge. This is done for day and night using the mean sensor zenith angle for each sampled 1° × 1° L3 grid box.

Day and night cloud LWP retrieved along trajectories comes from the AMSR-E sensor (Wentz and Meissner 2004) averaged to the 1° × 1° L3 grid. AMSR-E provides total LWP, which includes clear and cloudy portions, so total LWP is divided by MODIS cloud fraction to estimate the LWP for cloudy portions only (CLWP). This AMSR-E product is different from the MODIS LWP used to classify the MCC, which is only available during daytime. We choose the AMSR-E LWP as a tracked variable because of the availability of nighttime data. For LWP values below 0.18 kg m^{-2}, the AMSR-E algorithm does not distinguish between cloud water and rainwater, producing a high bias in cloud water path due to the inclusion of rainwater. In the appendix, we use rain rates produced using the AMSR-E 89-GHz brightness temperatures (introduced below) to create an adjusted LWP product with the estimated rainwater contribution removed. This study was done using both the adjusted and unadjusted CLWP product, with little qualitative difference in results.

Cloud droplet number concentration (N_d) estimates come from three sources: Our primary N_d dataset uses a combination of cloud droplet effective radius and liquid water path detected by the MODIS collection 6 daytime-only optical properties dataset (King et al. 2003) and the relationship developed by Boers et al. (2006) and Bennartz (2007) and shown as Eq. (1) in Possner et al. (2020). Two other N_d products are compared in section 3c: One was developed by Grosvenor and Wood (2018), which uses the collection 5 MODIS optical properties data and a different set of relationships. A third, independent, N_d data source is the Modern-Era Retrospective Analysis for Research and Applications, version 2 (MERRA-2; Gelaro et al. 2017), which provides estimates of aerosol concentrations for a variety of different aerosol types and sizes. These concentrations can be combined with the regression coefficients determined in D. T. McCoy et al. (2017) to estimate N_d. Because

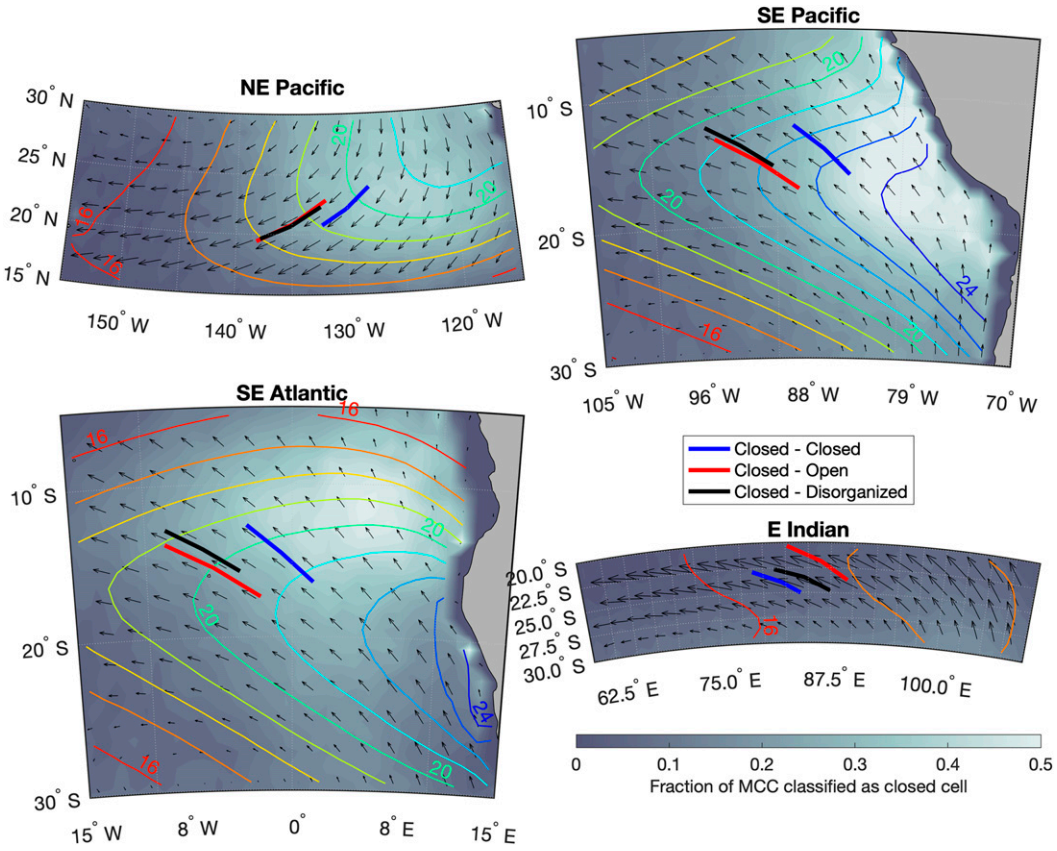

FIG. 3. Thick lines show the mean locations of composited 24-h trajectories for all three possible MCC transition types within each study region. Annual mean wind directions and relative speeds at 925 hPa are shown by the arrows. The colored line contours show the annual mean LTS. The shading shows the frequency of closed cell MCC relative to all classifications, with whiter shading indicating more closed cells.

of the difficult-to-retrieve nature of N_d and the possibilities of biases in the data associated with cloud edge retrievals, multiple N_d products are compared here to substantiate results.

Day and night rain rate estimates come from the routine introduced in Eastman et al. (2019), which uses the relationship between brightness temperature T_b observed by AMSR-E at 89 GHz and rain rate as measured by the rain-profile dataset (Mitrescu et al. 2010; Lebsock and L'Ecuyer 2011) from the *CloudSat* cloud profiling radar. Rain rate estimation relies on the positive relationship between T_b and rain rate (Miller and Yuter 2013), where warm T_b is associated with greater in-cloud LWP and heavier rain rates. The product is able to produce estimates of rain rate after controlling for three other variables that also drive T_b variation: surface wind speed, column water vapor, and sea surface temperature. Column water vapor is measured by the AMSR-E (Wentz and Meissner 2004). For the updated version of this precipitation dataset used here, SST and wind speed now come from the ERA5 reanalysis. Rain rates are resolved in 4 km × 6 km grid boxes, which is of a sufficient resolution to see most individual cellular elements in Sc cloud decks.

The depth of the PBL, assumed to be the same as the height of the trade inversion, is estimated using the difference between SST and cloud-top temperature for a subset of clouds with tops assumed to be at the base of the trade inversion. The depth of this layer is determined using a parameterized lapse rate from Wood and Bretherton (2004). The temperature of the clouds at inversion top is estimated using the algorithm developed in Eastman et al. (2016, 2017), which is tuned through a comparison between MODIS cloud-top temperature histograms and *CALIPSO* vertical feature mask data (Vaughan et al. 2004).

3. Results

a. Climatological behavior of transitions

A geographic comparison between our trajectory sets is shown in Fig. 3, where trajectories are composited by transition type within each region. Figure 3 also includes mean wind vectors at 925 hPa, the annual mean LTS, and a shaded contour showing the relative frequency of closed cell MCC in comparison with the other MCC types. The NE Pacific, SE Pacific, and SE Atlantic show similar results: closed–closed trajectories are seen farther upwind, in regions with a stronger inversion, while the closed–open and closed–disorganized transitions tend to occur farther offshore and are in comparable locations.

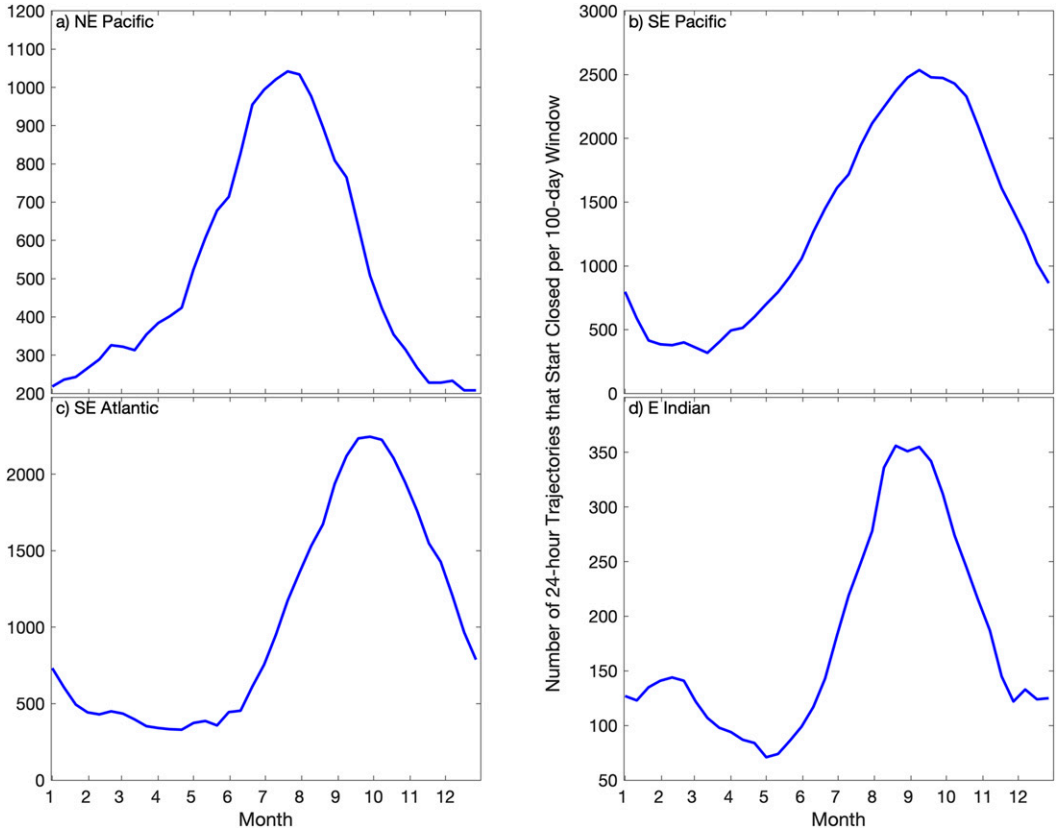

FIG. 4. The number of all available 24-h trajectories per 100-day sampling window (sampled every 10 days) that start as closed cells for years 2007–10, showing a strong yearly cycle of closed cells. The *y*-axis ranges differ for each region.

In contrast, the closed–open trajectories in the E Indian region tend to occur farther upwind and farther north while the closed–disorganized and closed–closed mean trajectories begin farther offshore.

The seasonality of closed cell transitions is explored in Figs. 4 and 5. Figure 4 shows the number of trajectories that begin as closed cells within a 100-day sampling window. A significant seasonal cycle is apparent in every region, with peaks in the early austral spring for the Southern Hemisphere regions, and in the early boreal summer for the NE Pacific.

In Fig. 5 the fraction of closed cells that break into open cells (red), break into disorganized cells (black), or stay closed (blue) are compared between regions. Trajectories remain closed more often when trajectories beginning as closed cell are more frequent (from Fig. 4). The fraction of closed cells that break into open cells is relatively stable throughout the year. In contrast, the fraction of closed cells that transition to disorganized is seasonally variable, corresponding with the opposing seasonality in the fraction of closed cells that remain closed. The lack of a seasonal cycle in the relative frequency of closed–open transitions is peculiar, given the strong seasonal cycles in most meteorological variables in these regions (Eastman et al. 2017, their Fig. 7) and may suggest that the closed–open transition has less sensitivity to seasonally varying meteorological conditions. This contrasts with the significant seasonal cycle in the relative frequency of the closed–closed and closed–disorganized transitions, which implies they may be driven by varying meteorological conditions. For example, LTS tends to be higher when closed–closed trajectories are most frequently observed in the NE Pacific, SE Pacific, and SE Atlantic (again from Eastman et al. 2017, their Fig. 7).

b. Composite analysis of cloud and predictor variables

Figures 6 and 7 show regional breakdowns of composited cloud and meteorological variables taken at 0, 12, and 24 h for our three trajectory sets. Composites represent averages of all trajectories exhibiting that transition type with the transition type specified by color. The width (in the *y* direction) of the plots represents the 2-sigma standard error, to allow comparison of means. Separation between the bounds indicates a greater than 95% confidence that the sample means are different. Cloud variables compared in Fig. 6 show that cloud cover (Figs. 6a,f,k,p) evolves similarly in each region, but differently for each set: closed–closed trajectories stay overcast, closed–open trajectories experience some cloud reduction, and closed–disorganized trajectories experience the most cloud loss. The sets remain overcast at the 0130 LT sampling time, indicating that the breakup into open and disorganized cells occurs between 0130 and 1330 LT. This timing is consistent with the conclusions from the analysis of a much more limited set of closed-to-open cell MCC transition cases in Wood et al.

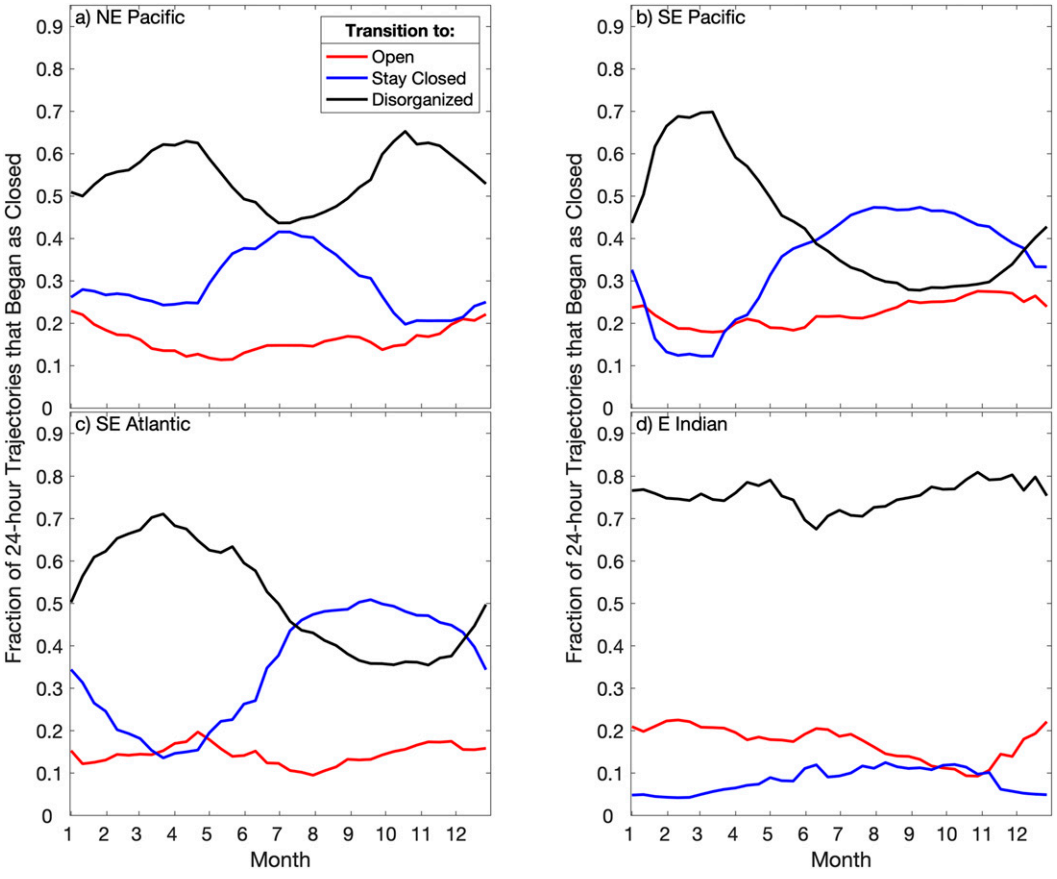

FIG. 5. The fraction of 24-h trajectories that begin as closed cells per 100-day sampling window (sampled every 10 days) that shows a specific transition in MCC classification for each study region.

(2008, their Fig. 10), which showed transitions peaking from 0300 to 0600 local time. For our other cloud variables, the NE Pacific, SE Pacific, and SE Atlantic show similar behavior. In those three regions closed–closed trajectories begin and end with the most N_d and the lightest rain rates, begin with less CLWP and begin in shallower PBLs. Relative to the other trajectory sets, closed–open trajectories have significantly lower N_d, greater overnight rain rates, and higher 0-h CLWP. Closed–disorganized trajectories begin in deeper PBLs, have less overnight CLWP, lower rain rates, and middling N_d relative to the other two sets. The E Indian ocean appears to be an outlier in Fig. 6, with less distinction between sets. The most significant difference between sets in the E Indian is the stronger rain rate seen throughout the evolution of the closed–open trajectories, which is in agreement with the rain behavior in the other regions.

Figure 7 shows composites of meteorological variables in the same manner as Fig. 6. In all regions except the SE Pacific, q_{700} is lowest for the closed–disorganized set. Wind speed is significantly higher for the closed–open set in all four regions. The sea surface is coolest and LTS is highest for the closed–closed sets in all four regions. Subsidence is lowest at 0 and 12 h for the closed–disorganized sets in the SE Pacific, SE Atlantic, and NE Pacific.

To further verify results, we remove the effects of mean geographical, seasonal, and diurnal differences between the trajectory sets by producing anomalies relative to the 100-day running mean of each variable centered on each day for day and night separately. Figures 8 and 9 show anomalies of our cloud and meteorological variables composited for all regions, respectively. Results using anomalies reinforce the results from Figs. 6 and 7 with stark contrasts present between the trajectory sets. Closed–open trajectories are associated with significantly stronger winds, reduced N_d, and heavier overnight rain. Closed–disorganized transitions are associated with reduced subsidence and LTS, a drier free troposphere, and warmer sea surface. This suggests that drivers of closed–open cell transitions are distinct from closed–disorganized transitions: closed–open transitions are associated with internal microphysical and precipitation processes along with stronger winds, while closed–disorganized transitions are driven by the surrounding meteorological conditions.

A comparison of Figs. 8 and 9 with the regional behaviors seen in Figs. 6 and 7 shows that the evolution of MCC within each region may be driven by somewhat different processes. For instance, there is little evidence that N_d is lower before the closed–open transition in the E Indian relative to the other transitions, but in the other three regions N_d is much lower

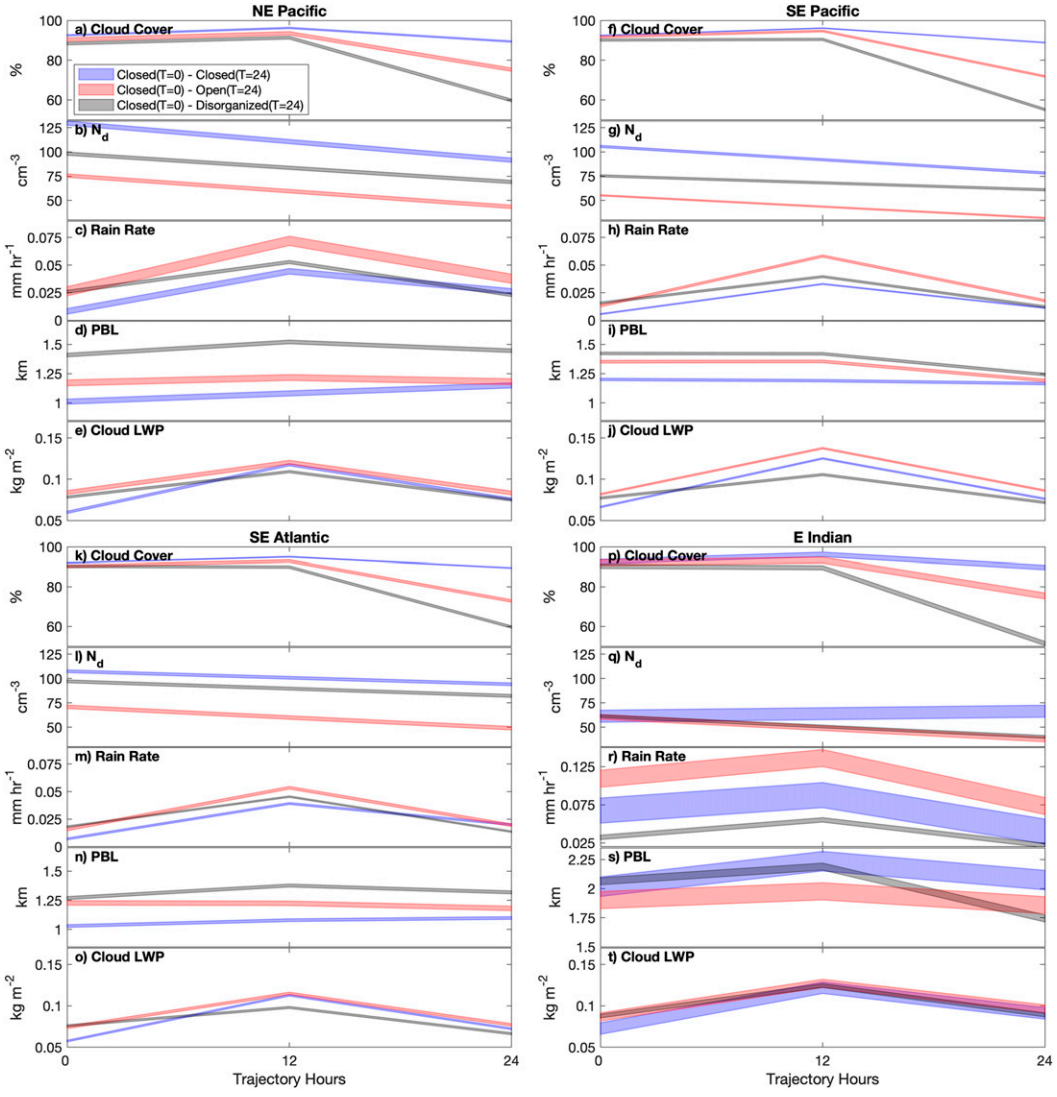

FIG. 6. Composited 24-h evolution of cloud variables for trajectories that begin as closed cells but evolve into open (red) cells or disorganized cells (black) or stay closed (blue), broken down by study region. Variables shown are (a),(f),(k),(p) cloud cover, (b),(g),(l),(q) cloud droplet number concentration, (c),(g),(m),(r) rain rate, (d),(h),(n),(s) planetary boundary layer depth, and (e),(i),(o),(t) cloud liquid water path. Plot width represents the 2σ standard error. The y-axis range is identical for the NE Pacific, SE Pacific, and SE Atlantic but different for the E Indian region.

prior to the closed–open transition. Instead, the E Indian closed–open transition is associated with much higher rain rates relative to the other transition types there, or the other regions. Combining all regions in Figs. 8 and 9 allows us to see these processes in aggregate, where differing dominant processes in different regions are combined. Looking into a single region, or excluding any regions, may cause a study to miss out on relevant mechanics.

Typically, subtropical Sc PBLs deepen at night due to the increased turbulence and entrainment driven by radiative cooling at cloud top. However, Fig. 8d illustrates shallower PBL depth anomalies at night for closed–closed and closed–open trajectories when compared with closed–disorganized. Further, Figs. 6d, 6i, 6n, and 6s show closed–closed and closed–open sets have less change in PBL depth over 24 h than do closed–disorganized sets. This difference in cycles is likely due to differences in q_{700}, subsidence, and inversion strength seen between the trajectory sets in Fig. 9. Taken together, these differences in meteorological conditions for the closed–disorganized set drive: Increased cloud-top cooling through a drier free troposphere, stronger entrainment across a weaker inversion, and more PBL deepening given the weaker compensating downward motion in the troposphere. All of these processes suggest that the clouds are experiencing warming and drying through entrainment of free-tropospheric air. The closed–open transition exhibits an enhanced diurnal cycle in

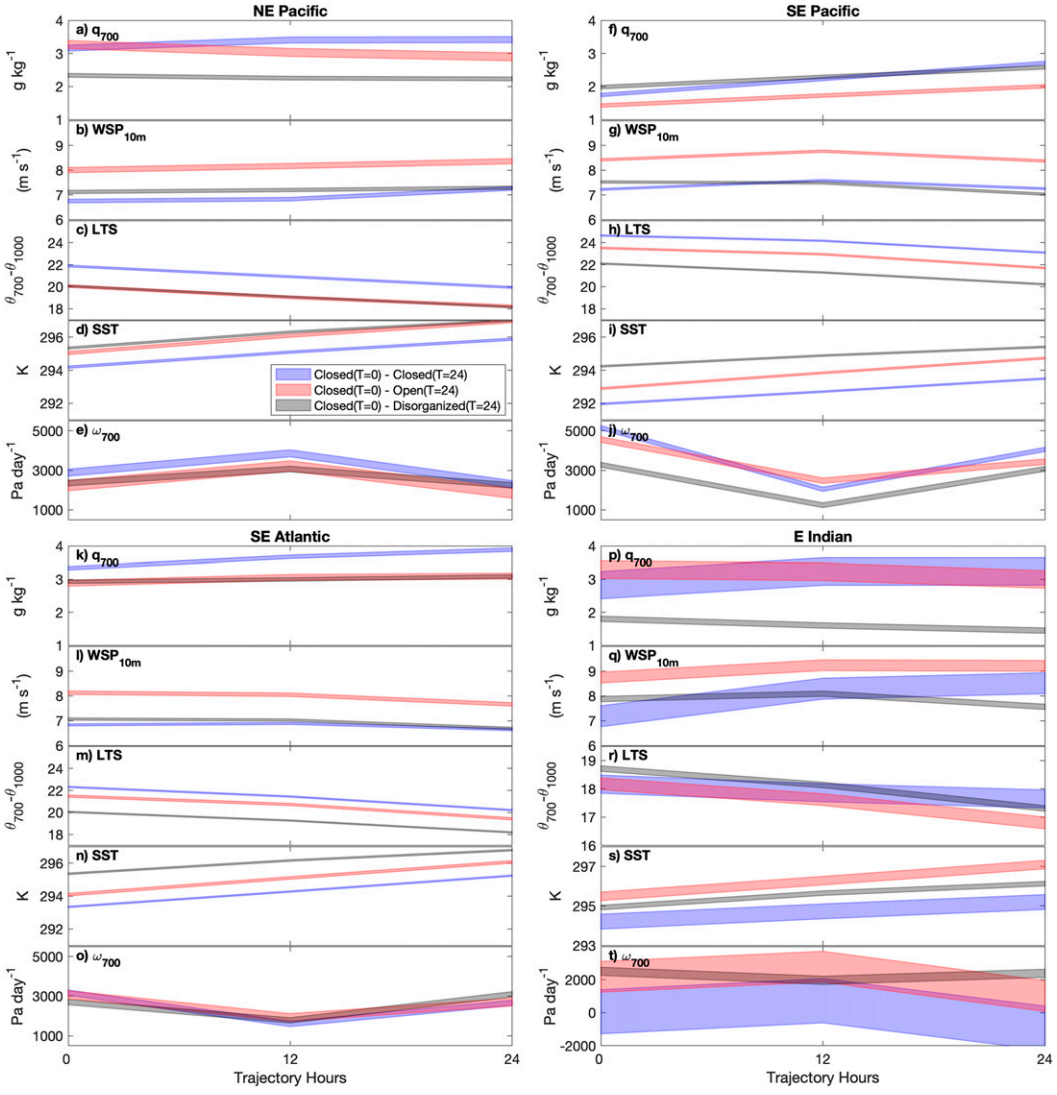

FIG. 7. Composited 24-h evolution of environmental variables for trajectories that begin as closed cells but evolve into open (red) cells or disorganized cells (black) or stay closed (blue), broken down by region. Variables shown are (a),(f),(k),(p) 700-hPa specific humidity, (b),(g),(l),(q) 10-m wind speed, (c),(g),(m),(r) lower-tropospheric stability (θ_{700}–θ_{1000}), (d),(h),(n),(s) sea surface temperature, and (e),(i),(o),(t) 700-hPa subsidence. Plot width represents the 2σ standard error. The *y*-axis range is identical for the NE Pacific, SE Pacific, and SE Atlantic but different for the E Indian region.

precipitation and LWP. This suggests that overnight precipitation processes may drive the cloud evolution instead of the drying through PBL deepening and entrainment seen in the contrasting closed–disorganized cases. These results are summarized in Table 1, which shows the cloud and meteorological variables most strongly associated with the three MCC transitions examined in our study.

c. *Untangling rain and N_d*

Interpreting the evolution of rain rate and N_d along Lagrangian trajectories requires more care as the calculations of these values are nuanced and entangled. This is in part because rain rate and N_d tend to strongly covary. Cloud drops tend to be large and drop concentrations tend to be low when rain is present. Additionally, the routines and source data used to estimate N_d from satellite observations may introduce biases due to the application of a single routine to distinct cloud regimes with distinct vertical variations of N_d (Fu et al. 2019). Here, we attempt to untangle these issues by first comparing three different N_d products in our compositing routine. Then, we further divide trajectories into groups/sets in which either precipitation or N_d is held somewhat constant while the other variable is unconstrained, allowing for the effects of one to be tested while the other is controlled.

The N_d analysis from Fig. 6b, 6g, 6l, and 6q is repeated for all regions combined using three separate N_d datasets: our default

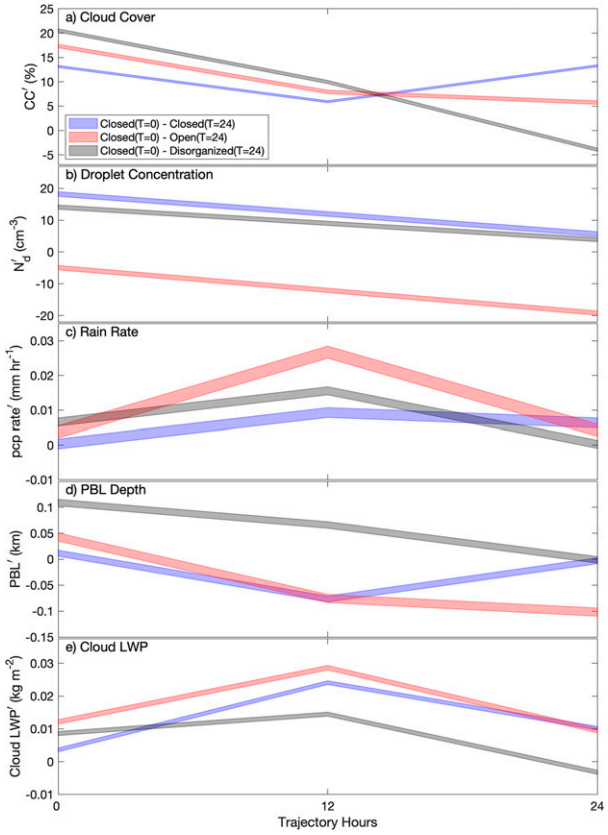

FIG. 8. Composited 24-h evolution of anomalies of cloud variables for trajectories that begin as closed cells but evolve into open (red) cells or disorganized cells (black) or stay closed (blue). Cloud variables include (a) cloud cover, (b) cloud droplet number concentration, (c) rain rate, (d) planetary boundary layer depth, and (e) in-cloud liquid water path. Anomalies are calculated by removing the 100-day running mean centered on each day in each $1° \times 1°$ grid box for day and night separately. Plot width represents the 2σ standard error.

N_d (Fig. 10a), the N_d from Grosvenor and Wood (2018) (hereinafter "Grosvenor N_d"; Fig. 10b), and, as an entirely independent data source, the N_d derived from MERRA aerosol reanalysis using the regression established by D. T. McCoy et al. (2017) (Fig. 10c). The default N_d dataset relies on MODIS C6 data, while the Grosvenor N_d uses MODIS C5, creating some degree of independence, though they are both derived from the same sensor. The Grosvenor N_d is specifically suited to single layer, mostly overcast Sc, making it best suited for the comparison at 0 h when all trajectories are closed cell, but less suited for the later observations where clouds have broken up.

The separation of groups in all three frames of Fig. 10 supports our result, showing that closed–open transitions are associated with fewer N_d at the outset and closed–closed trajectories have higher N_d. The Grosvenor N_d shows a higher mean and increasing tendency for the closed–disorganized set, which is at odds with the other two products, although this tendency is only based on two data points. This increase in Grosvenor N_d is likely due to the increasingly broken clouds over time in the closed–disorganized transition. The Grosvenor N_d is calculated for clouds that are primarily overcast, so the subset of observations that we show that are disorganized and also mostly overcast here represents a very small, and somewhat peculiar slice of our data. A closer look shows that there are 838 closed–disorganized transitions sampled for the Grosvenor N_d, while the other two products have over 4800. This makes the Grosvenor N_d less robust for this set and is likely why the mean and tendency is in disagreement with the other products. However, again, it is unwise inferring much from slopes derived from two data points.

In Fig. 11 we attempt to untangle the covarying effects of rain and N_d. Here, our trajectory sets are grouped into quantiles based on 0-h precipitation probability or N_d. Composites for the covarying variable from our three trajectory sets (closed–closed, closed–open, closed–disorganized) are compared to see whether their behavior is different when their covarying variable is constrained. Results from Figs. 11a–d show that reduced 0-h N_d is associated with the closed–open transition regardless of whether rain is likely at 0 h. This was repeated for overnight (12 h) rain observations, and the results were qualitatively identical, indicating that N_d may influence the closed–open transition independently of rain. Figures 11e–h show that rainfall appears significantly associated with the closed–open transition for three of the four sets. The rainfall signal was present, but not significant when N_d was very low (below 27 cm^{-3}, from the default C6 product). Figures 11e–h indicate, as above, that rain may influence the closed–open transition independently of N_d. These results suggest that either rain and N_d may be associated with separate mechanisms driving the closed–open transition, or they may be a symptom of another mechanism that drives the transition while also modifying both N_d and rain rate.

4. Discussion

Prior work has shown a positive connection between heavier precipitation, depleted N_d, and the appearance of open MCC clouds using observations (Rosenfeld et al. 2006; Wood et al. 2008) and models (Wang and Feingold 2009; Feingold et al. 2015; Savic-Jovcic and Stevens 2008). Here, we substantiate these findings with a larger, more statistically robust dataset that comprises tens of thousands of observations. We also analyze a time dimension showing that negative N_d anomalies and positive precipitation anomalies *precede* the transition from closed to open MCC clouds. In addition to the established microphysical and precipitation connections, this work shows that faster surface wind speeds are associated with the closed–open transition.

In comparing the closed–open transition with transitions from closed to disorganized MCC, we show that the former is physically distinct from the latter. Transitions from closed–open MCC occur in PBLs that are environmentally similar to PBLs where MCC remain closed cell. However, different internal microphysical and precipitation properties are present in the closed–open transition, as suggested by Wood and Hartmann (2006). Thus, open cells can be considered a special expression of the Sc boundary layer. In contrast, the closed–disorganized MCC transition is driven by meteorological

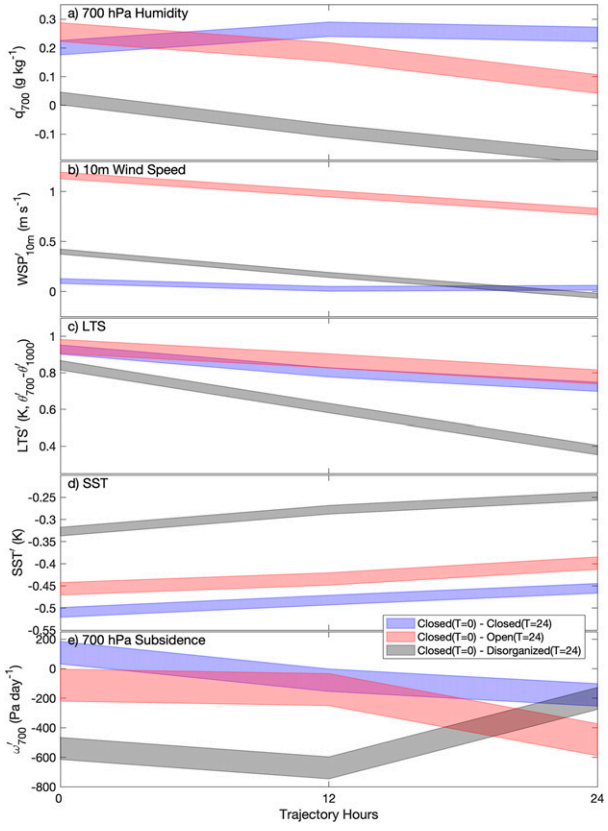

FIG. 9. Composited 24-h evolution of anomalies of environmental variables for trajectories that begin as closed cells but evolve into open (red) cells or disorganized cells (black) or stay closed (blue). Environmental variables include (a) 700-hPa specific humidity, (b) 10-m wind speed, (c) lower-tropospheric stability (θ_{700}–θ_{1000}), (d) sea surface temperature, and (e) 700-hPa subsidence. Anomalies are calculated by removing the 100-day running mean centered on each day in each 1° × 1° grid box for day and night separately. Plot width represents the 2σ standard error.

conditions surrounding the PBL, where processes act to warm and dry the cloud deck.

Christensen et al. (2020) shows that high N_d prolongs Sc lifetime. Using this Lagrangian analysis coupled with MCC classifications, we show that Sc that remain as closed cell prefer high-N_d environments. This result suggests that the Christensen et al. (2020) result may be in part driven by fewer closed–open transitions when N_d is high. This is also in agreement with the results from Rosenfeld et al. (2006), which show that closed cells remain in ship tracks through fields of open cell MCC and conclude that cellular transitions from closed to open are highly sensitive to cloud droplet concentrations.

Results here are limited to the large-scale meteorological variables and cloud deck conditions associated with MCC transitions seen by our trajectories. We have identified three of our tested variables as being associated with closed–open transitions, either prior to the transition in the case of reduced N_d and stronger wind speed, or concurrent with the overnight transition in the case of heavier rain. These results can aid in predicting the likelihood of closed–open transitions or in establishing more realistic boundary conditions in models that study the transition, but they do not directly reveal an exact mechanism for the closed–open transition. The overnight PBL deepening and entrainment drying hypothesis for the closed–disorganized transitions appears to be well supported by the data. The closed–disorganized transition usually occurs farther downstream, closer to the equatorial edge, with a warmer sea surface and weaker stability. A corresponding mechanism for the closed–open transition is less clear but is likely associated with the high overnight rain rates and likely aided by increased wind speed and low N_d.

Future work may focus specifically on the closed–open transition, which occurs in similar boundary layers with similar meteorological conditions to the unchanged closed–closed trajectories, but with stronger surface winds and different microphysics and rainfall characteristics. Some questions motivated by our results are as follows: Is wind speed a driver of the closed–open transition, does wind speed have a strong effect on microphysics and/or precipitation, are synoptic differences apparent between longer back trajectories, and what drives the higher LWP and reduced N_d that tends to precede closed–open transitions? Prior observational work in pristine marine Cu appears to show that stronger wind is associated with more cloud drops (Colón-Robles et al. 2006), though that focuses on different geographical regimes (and perhaps different cloud processes) than we do here. Kazil et al. (2016) modeled nonprecipitating Sc for a variety of wind speeds and show a stronger LWP diurnal cycle, and higher LWP on average when wind is stronger. This is due to enhanced surface moisture fluxes and increased production of turbulent kinetic energy (TKE) in buoyant updrafts, which could be part of the mechanism driving the closed–open transition, though a study including precipitation would be beneficial. A higher latent heat flux associated with stronger winds would lead to greater condensation and stronger buoyant production of TKE (as explained in Bretherton and Wyant 1997). Scott et al. (2020) go on to show that stronger winds in subtropical Sc regions are associated with enhanced cloud amount, but decreasing optical thickness, which *could* hint at changes in cellular structure. The positive connection between surface wind speed and open cells was mentioned in Wood et al. (2008); however, a detailed analysis is lacking. Bony et al. (2020) also see that patterns of mesoscale cloud organization are well separated by wind speed in the tropics. It is possible that other characteristics associated with stronger winds are mechanically responsible for the transition: convergence/divergence, shear within the PBL or across the inversion, or additional turbulence within the PBL. Future work concerning the closed–open transition will incorporate longer trajectories to study the boundary layer for several days prior to transition to see whether microphysical anomalies are organized around perturbations in the flow, or whether flow perturbations could be influenced by precipitation or microphysical processes in the clouds. Higher temporal sampling resolution of reanalysis variables is also a priority moving forward.

The analysis in section 3c begins to untangle rain and N_d, suggesting that heavy rain and reduced N_d are independently

TABLE 1. The environmental and cloud variables most strongly associated with our three 24-h MCC transitions.

Closed–closed	Closed–open	Closed–disorganized
Shallow PBL	—	Deep PBL
High N_d	Low N_d	—
Low rain rate	Heavier overnight drizzle	—
Cool SST	—	Warm SST
High LTS	—	Low LTS
—	Strong wind speed	—
—	—	Dry free troposphere
—	—	Weak subsidence

associated with trajectories that transition from closed–open MCC. A limitation of this analysis is that we only observe precipitation at 12-h intervals, with only one overnight observation at 0130 local time. Rainfall may be present before or after this observation, making it possible that all transitions are associated with rain, but not all of the rain is observed. Studies using geostationary satellite data, large-eddy-simulating models, or higher-resolution in situ studies (such as Abel et al. 2020) could aid in determining whether separate mechanisms exist for the closed–open transition, or whether a single mechanism explains the differences in rain, N_d, and wind speed.

The geographic limitation of this study raises questions as to whether the nature of the transitions seen in the subtropical eastern ocean regions is common to other regions. Future work should study transitions in MCC in a range of climatological regions, which may better elucidate a set of mechanisms associated with transitions. Transitions in remote midlatitude oceans may be free of N_d-altering pollution near the coasts and may also occur where wind speeds are more variable, offering a wider sampling of wind conditions and perhaps better constraints on N_d. Further, midlatitude transitions are more likely to be synoptically driven, so understanding these meteorological mechanics will create a clearer, more robust understanding of MCC types and transitions.

In Eastman and Wood (2016) it was shown that rainfall had little effect on Lagrangian changes in Sc cloud amount. Now that cellular structure can be assessed alongside cloud amount, that result can be clarified: Rainfall does appear associated with the Lagrangian closed–open cell transition, but less so for the closed–disorganized transition. The closed–disorganized MCC transition is more than 2 times as common as the closed–open transition and is associated with a greater decline in cloud amount. Therefore, it is likely that the closed–disorganized signal obscured the weaker, less frequent closed–open signal in that work. The new results presented here show that it is imperative that cloud cellular structure be assessed alongside cloud amount if the goal is to properly capture cloud processes.

5. Conclusions

Mesoscale cellular convection (MCC) is classified into three groups using a machine learning algorithm: Closed cell, open cell, and cellular but disorganized. Classifications of MCC type are sampled along 24-h trajectory segments, beginning

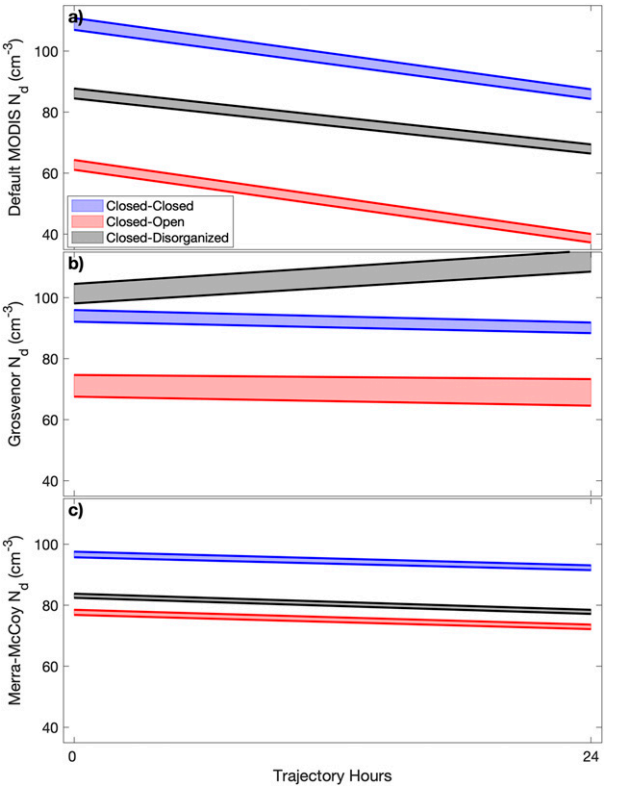

FIG. 10. The 24-h evolution of N_d composited for our three trajectory sets (blue: closed–closed; red: closed–open; black: closed–disorganized) for three different N_d products: (a) our default product, (b) Grosvenor and Wood (2018) N_d from MODIS c5, and (c) D. T. McCoy et al. (2017) MERRA aerosol regression N_d. Plot width represents the 2σ standard error. Droplet concentration values must be present at both 0 and 24 h for a trajectory to contribute to the composite.

and ending at 1330 LT, and sampled every 12 h by A-Train satellites and ERA-Interim reanalysis fields. Three trajectory sets are analyzed, all of which begin as closed cells and either stay closed, transition into open cells, or transition into disorganized cells.

A geographical comparison of the mean locations of transition types in our four subtropical ocean study regions shows similar mean behaviors in the NE Pacific, SE Pacific, and SE Atlantic regions. In those three regions closed–closed trajectories tend to exist closer to the coasts where LTS is climatologically greater, whereas closed–open and closed–disorganized transitions occur farther offshore. The E Indian region behaves in the opposite way, with closed–open occurring closest to shore and closed–closed farthest offshore. These geographic distributions may be in part due to the geographic distributions in the training dataset, which could influence the output of the algorithm.

A seasonal analysis shows that trajectories that begin as closed cells are more common in the spring in our Southern Hemisphere regions, and in summer in the NE Pacific. A seasonal breakdown of the fraction of trajectories that stay

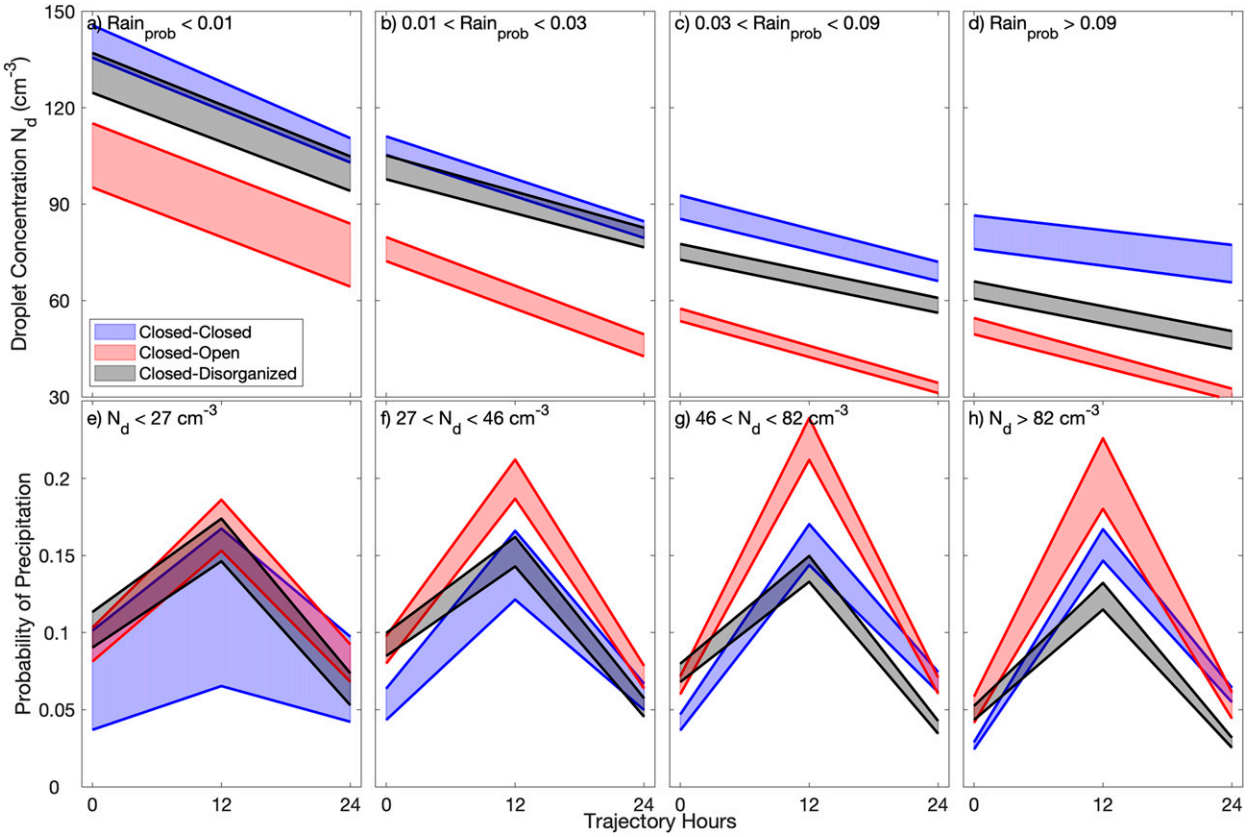

FIG. 11. A closer look at composited trajectories showing the 24-h changes of N_d and average precipitation probability for sets of trajectories beginning as closed cells. Trajectories are divided into quantiles on the basis of 0-h values of (a)–(d) precipitation probability and (e)–(h) N_d to show how one evolves while the other is constrained in quantile bins. The precipitation spike at 12 h is associated with the diurnal cycle of stratocumulus drizzle, which peaks at night more strongly for trajectories that transition from closed to open. Plot width represents the 2σ standard error.

closed as opposed to breaking into open or disorganized shows a strong trade-off between closed–closed and closed–disorganized MCC, whereas the fraction of trajectories that transition to open remains more constant throughout the year. The trade-off between closed–closed and closed–disorganized transitions hints at meteorological forcing driving the closed–disorganized transition. Specifically, the seasonal cycle of closed–closed/closed–disorganized MCC appears synchronized with LTS, which is highest when closed cells tend to remain closed.

A comparison of meteorological and cloud variables as drivers of MCC change shows significantly different conditions associated with closed–disorganized versus closed–open transitions (Table 1). Transitions to disorganized cells are associated with a stronger diurnal cycle of PBL depth, showing a greater amount of overnight deepening. This is likely driven by the accompanying weaker subsidence, weaker inversion, and drier free troposphere, which allows for enhanced entrainment of dry air into the cloud deck, causing drying and breakup. This contrasts significantly with the closed–open transition, which is associated with reduced N_d, stronger surface winds, and enhanced overnight precipitation in PBLs that begin as meteorologically comparable to the closed–closed set. A cursory analysis suggests that low N_d and heavier overnight rain may independently lead to the closed–open transition. Follow-on analyses are strongly motived to untangle the effects of wind speed, N_d, and rain on the closed–open transition, with the goal of discovering mechanism(s) that drive this transition.

Acknowledgments. This work was supported by NASA Grant 80NSSC19K1274. Research by author McCoy is supported by the NOAA Climate and Global Change Postdoctoral Fellowship Program, administered by UCAR's Cooperative Programs for the Advancement of Earth System Science (CPAESS) under Award NA18NWS4620043B. UCAR is sponsored by the National Science Foundation. The authors also thank Johannes Mohrmann for helpful discussion. AMSR data are produced by Remote Sensing Systems and were sponsored by the NASA AMSR-E Science Team and the NASA Earth Science MEaSUREs Program.

Data availability statement. ERA Interim data used here are available at https://doi.org/10.1002/qj.828 and are as in Dee

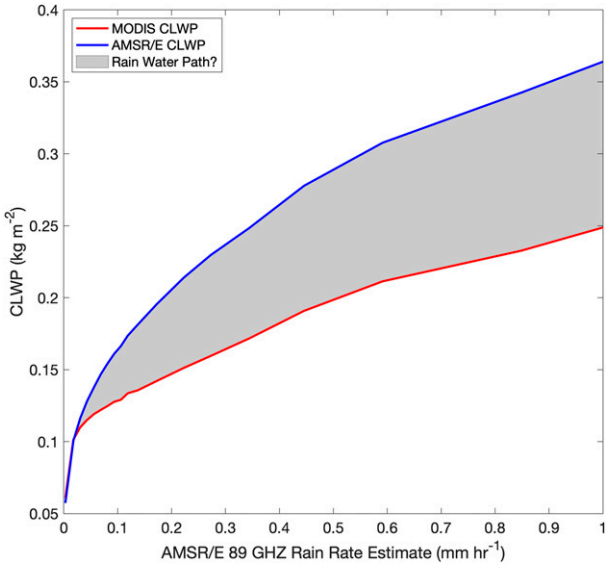

FIG. A1. MODIS 3.7-μm (red) and AMSR-E (blue) CLWP as a function of *CloudSat* and AMSR-E 89-GHz rain rates. The gray area represents the high bias in AMSR-E CLWP that is likely caused by rainwater and is plotted in Fig. A2 as a function of rain rate.

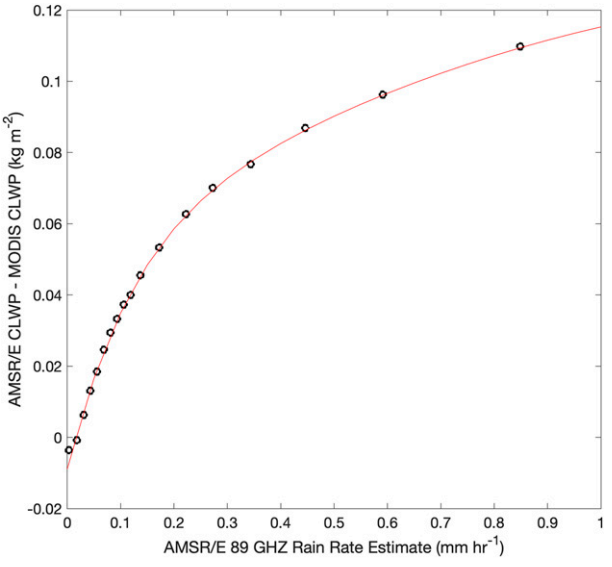

FIG. A2. The difference between AMSR-E and MODIS CLWP as a function of rain rate (black dots), with a seventh-degree polynomial fit to the points (red line).

et al. (2011). ERA5 data (https://doi.org/10.5065/D6X34W69) used are available at https://apps.ecmwf.int/data-catalogues/era5/?class=ea. MODIS collection 6 L3 data are available at https://doi.org/10.5067/MODIS/MYD08_D3.006. MODIS collection 6 L2 data are available at https://doi.org/10.5067/MODIS/MYD06_L2.006. AMSR-E L3 gridded day and night averages from Wentz et al. (2014) are available at http://www.remss.com/missions/amsr. AMSR-E 89-GHz brightness temperatures from Ashcroft and Wentz (2019) are available at https://doi.org/10.5067/YL62FUZLAJUT. *CloudSat* rain-profile (Lebsock and L'Ecuyer 2011) data are available at http://www.cloudsat.cira.colostate.edu/data-products/level-2c/2c-rain-profile. *CALIPSO* vertical feature mask data are available at https://eosweb.larc.nasa.gov/project/calipso/lidar_l2_vfm_table. The observed PBL and rain rate estimate data are processed using the above datasets and are also available from the author upon request.

APPENDIX

Creation of an Adjusted LWP Product

By design, the AMSR-E passive microwave LWP product fails to distinguish between cloud water and rainwater until LWP exceeds 0.18 kg m^{-2}. At that threshold, a partitioning is imposed, assuming that cloud liquid water is a function of rain rate and the depth of the rain column. The inclusion of drizzle and rain in the calculation of CLWP for values below 0.18 km m^{-2} introduces a high bias in CLWP relative to other products, such as the daytime-only MODIS CLWP, which is based on cloud-top optical properties and not passive microwave retrievals. This is shown in Greenwald et al. (2018, their Fig. 3) where AMSR-E CLWP and MODIS CLWP calculated from the 3.7-μm channel are plotted as a function of AMSR-E total liquid water path (TLWP). In that plot, the mean AMSR-E CLWP is higher than MODIS CLWP for TLWP values above ~0.03 kg m^{-2}. This high bias is likely due to the inclusion of drizzle in the AMSR-E CLWP, so the separation of the curves for TLWP values below 0.18 kg m^{-2} may be in large part due to the unaccounted-for presence of drizzle and rain drops.

Now with the availability of a semi-independent rain-rate product, the *CloudSat* and AMSR-E 89-GHz rain rate estimates used in this work, we can recreate this plot (Greenwald et al. 2018, Fig. 3) for values of CLWP as a function of rain rate for averages in 1° × 1° L3 grid boxes, shown in Fig. A1. We use the coarse L3 grid boxes to mitigate the effects of rainfall in neighboring AMSR-E pixels, which also have an effect on AMSR-E CLWP. The gray area between the two curves represents the high bias in AMSR-E CLWP relative to MODIS. It is likely that this high bias is caused by the inclusion of rain and drizzle drops in the AMSR-E product. This bias begins to affect AMSR-E CLWP values for rain rates above 0.03 mm h^{-1}.

The high bias in AMSR/E is approximated as a function of rain rate and can be accounted for. The difference between the two curves in Fig. A1 is shown in Fig. A2, where a polynomial is fit to the data points for rain rates below 1 mm h^{-1}. The removal of the effects of rainwater is done by estimating the CLWP bias in AMSR-E as a function of 89-GHz rain rate (using the polynomial from Fig. 2) for all drizzling L3 grid boxes, then subtracting this estimated bias from the AMSR-E CLWP values, leaving an adjusted CLWP with the effects of precipitation reduced. This adjusted value is used here. For rain rates above 1 mm h^{-1}, there are too few data points to extend the curve, so those values are eliminated. This removes less than 0.008% of our grid boxes.

REFERENCES

Abel, S. J., and Coauthors, 2020: Open cells exhibit weaker entrainment of free-tropospheric biomass burning aerosol into the south-east Atlantic boundary layer. *Atmos. Chem. Phys.*, **20**, 4059–4084, https://doi.org/10.5194/acp-20-4059-2020.

Agee, E. M., 1987: Mesoscale cellular convection over the oceans. *Dyn. Atmos. Oceans*, **10**, 317–341, https://doi.org/10.1016/0377-0265(87)90023-6.

Ashcroft, P., and F. J. Wentz, 2019: AMSR-E/*Aqua* L2A global swath spatially-resampled brightness temperatures, version 4 (89 GHz). NASA National Snow and Ice Data Center Distributed Active Archive Center, accessed 15 October 2020, https://doi.org/10.5067/YL62FUZLAJUT.

Bender, F. A.-M., A. Engström, and J. Karlsson, 2016: Factors controlling cloud albedo in marine subtropical stratocumulus regions in climate models and satellite observations. *J. Climate*, **29**, 3559–3587, https://doi.org/10.1175/JCLI-D-15-0095.1.

Bennartz, R., 2007: Global assessment of marine boundary layer cloud droplet number concentration from satellites. *J. Geophys. Res.*, **112**, D02201, https://doi.org/10.1029/2006JD007547.

Boers, R., J. A. Acarreta, and J. L. Gras, 2006: Satellite monitoring of the first indirect aerosol effect: Retrieval of the droplet concentration of water clouds. *J. Geophys. Res.*, **111**, D22208, https://doi.org/10.1029/2005JD006838.

Bony, S., H. Shultz, J. Vial, B. Stevens, 2020: Sugar, gravel, fish, and flowers: Dependence of mesoscale patterns of trade-wind clouds on environmental conditions. *Geophys. Res. Lett.*, **47**, e2019GL085988, https://doi.org/10.1029/2019GL085988.

Bretherton, C. S., and M. C. Wyant, 1997: Moisture transport, lower-tropospheric stability, and decoupling of cloud-topped boundary layers. *J. Atmos. Sci.*, **54**, 148–167, https://doi.org/10.1175/1520-0469(1997)054<0148:MTLTSA>2.0.CO;2.

——, R. Wood, R. C. George, D. Leon, G. Allen, and X. Zheng, 2010: Southeast Pacific stratocumulus clouds, precipitation and boundary layer structure sampled along 20 S during VOCALS-Rex. *Atmos. Chem. Phys.*, **10**, 10 639–10 654, https://doi.org/10.5194/acp-10-10639-2010.

Christensen, M. W., W. K. Jones, and P. Stier, 2020: Aerosols enhance cloud lifetime and brightness along the stratus-to-cumulus transition. *Proc. Natl. Acad. Sci. USA*, **117**, 17 591–17 598, https://doi.org/10.1073/pnas.1921231117.

Colón-Robles, M., R. M. Rauber, and J. B. Jensen, 2006: Influence of low level wind speed on droplet spectra near cloud base in trade wind cumulus. *Geophys. Res. Lett.*, **33**, L20814, https://doi.org/10.1029/2006GL027487.

Copernicus Climate Change Service, 2017: ERA5: Fifth generation of ECMWF atmospheric reanalyses of the global climate. Copernicus Climate Change Service CDS, accessed 15 September 2020, https://cds.climate.copernicus.eu/cdsapp#!/home.

Dee, D. P., and Coauthors, 2011: The ERA-Interim reanalysis: Configuration and performance of the data assimilation system. *Quart. J. Roy. Meteor. Soc.*, **137**, 553–597, https://doi.org/10.1002/qj.828.

Denby, L., 2020: Discovering the importance of mesoscale cloud organization through unsupervised classification. *Geophys. Res. Lett.*, **47**, e2019GL085190, https://doi.org/10.1029/2019GL085190.

Eastman, R., and R. Wood, 2016: Factors controlling low-cloud evolution over the eastern subtropical oceans: A Lagrangian perspective using the A-Train satellites. *J. Atmos. Sci.*, **73**, 331–351, https://doi.org/10.1175/JAS-D-15-0193.1.

——, and ——, 2018: The competing effects of stability and humidity on subtropical stratocumulus entrainment and cloud evolution from a Lagrangian perspective. *J. Atmos. Sci.*, **75**, 2563–2578, https://doi.org/10.1175/JAS-D-18-0030.1.

——, ——, and C. S. Bretherton, 2016: Time scales of clouds and cloud-controlling variables in subtropical stratocumulus from a Lagrangian perspective. *J. Atmos. Sci.*, **73**, 3079–3091, https://doi.org/10.1175/JAS-D-16-0050.1.

——, ——, and K. T. O, 2017: The subtropical stratocumulus-topped planetary boundary layer: A climatology and the Lagrangian evolution. *J. Atmos. Sci.*, **74**, 2633–2656, https://doi.org/10.1175/JAS-D-16-0336.1.

——, M. Lebsock, and R. Wood, 2019: Warm rain rates from AMSR-E 89-GHz brightness temperatures trained using *CloudSat* 380 rain-rate observations. *J. Atmos. Oceanic Technol.*, **36**, 1033–1051, https://doi.org/10.1175/JTECH-D-18-0185.1.

Feingold, G., I. Koren, T. Yamaguchi, and J. Kazil, 2015: On the reversibility of transitions between closed and open cellular convection. *Atmos. Chem. Phys.*, **15**, 7351–7367, https://doi.org/10.5194/acp-15-7351-2015.

Fu, D., L. Di Girolamo, L. Liang, and G. Zhao, 2019: Regional biases in MODIS marine liquid water cloud drop effective radius deduced through fusion with MISR. *J. Geophys. Res. Atmos.*, **124**, 13 182–13 196, https://doi.org/10.1029/2019JD031063.

Gelaro, R., and Coauthors, 2017: The Modern-Era Retrospective Analysis for Research and Applications, version 2 (MERRA-2). *J. Climate*, **30**, 5419–5454, https://doi.org/10.1175/JCLI-D-16-0758.1.

Greenwald, T. J., R. Bennartz, M. Lebsock, and J. Teixeira, 2018: An uncertainty data set for passive microwave satellite observations of warm cloud liquid water path. *J. Geophys. Res. Atmos.*, **123**, 3668–3687, https://doi.org/10.1002/2017JD027638.

Grosvenor, D. P., and R. Wood, 2018: Daily MODIS (Moderate Imaging Spectroradiometer) derived cloud droplet number concentration global dataset for 2003–2015. Centre for Environmental Data Analysis, accessed 15 August 2020, https://catalogue.ceda.ac.uk/uuid/cf97ccc802d348ec8a3b6f2995dfbbff.

Guichard, F. and F. Couvreux, 2017: A short review of numerical cloud-resolving models. *Tellus*, **69A**, 1373578, https://doi.org/10.1080/16000870.2017.1373578.

Hahn, C. J., and S. G. Warren, 2007: A gridded climatology of clouds over land (1971–1996) and ocean (1954–1997) from surface observations worldwide [updated 2009]. CDIAC Numeric data package NDP-026E, accessed 15 August 2020, https://atmos.uw.edu/CloudMap/NDP-026E_home.html.

Hartmann, D., M. E. Ockert-Bell, and M. L. Michelsen, 1992: The effect of cloud type on Earth's energy balance: Global analysis. *J. Climate*, **5**, 1281–1304, https://doi.org/10.1175/1520-0442(1992)005<1281:TEOCTO>2.0.CO;2.

Hubanks, P. A., M. D. King, S. Platnick, and R. Pincus, 2008: MODIS atmosphere L3 gridded product. NASA Algorithm Theoretical Basis Doc. ATBD-MOD-30, 90 pp.

Kazil, J., G. Feingold, and T. Yamaguchi, 2016: Wind speed response of marine non-precipitating stratocumulus clouds over a diurnal cycle in cloud-system resolving simulations. *Atmos. Chem. Phys.*, **16**, 5811–5839, https://doi.org/10.5194/acp-16-5811-2016.

King, M. D., and Coauthors, 2003: Cloud and aerosol properties, precipitable water, and profiles of temperature and water vapor from MODIS. *IEEE Trans. Geosci. Remote Sens.*, **41**, 442–458, https://doi.org/10.1109/TGRS.2002.808226.

Klein, S. A., 1997: Synoptic variability of low-cloud properties and meteorological parameters in the subtropical trade wind boundary layer. *J. Climate*, **10**, 2018–2039, https://doi.org/10.1175/1520-0442(1997)010<2018:SVOLCP>2.0.CO;2.

——, A. Hall, J. R. Norris, and R. Pincus, 2017: Low-cloud feedbacks from cloud-controlling factors: A review. *Surv. Geophys.*, **38**, 1307–1329, https://doi.org/10.1007/s10712-017-9433-3.

Lebsock, M. D., and T. S. L'Ecuyer, 2011: The retrieval of warm rain from *CloudSat*. *J. Geophys. Res.*, **116**, D20209, https://doi.org/10.1029/2011JD016076.

L'Ecuyer, T. S., Y. Hang, A. V. Matus, and Z. Wang, 2019: Reassessing the effect of cloud type on Earth's energy balance in the age of active spaceborne observations. Part I: Top of atmosphere and surface. *J. Climate*, **32**, 6197–6217, https://doi.org/10.1175/JCLI-D-18-0753.1.

Maddux, B. C., S. A. Ackerman, and S. Platnick, 2010: Viewing geometry dependencies in MODIS cloud products. *J. Atmos. Oceanic Technol.*, **27**, 1519–1528, https://doi.org/10.1175/2010JTECHA1432.1.

McCoy, D. T., F. A. M. Bender, J. K. C. Mohrmann, D. L. Hartmann, R. Wood, and D. P. Grosvenor, 2017: The global aerosol-cloud first indirect effect estimated using MODIS, MERRA, and AeroCom. *J. Geophys. Res. Atmos.*, **122**, 1779–1796, https://doi.org/10.1002/2016JD026141.

McCoy, I. L., R. Wood, J. K. Fletcher, 2017: Identifying meteorological controls on open and closed mesoscale cellular convection associated with marine cold air outbreaks. *J. Geophys. Res. Atmos.*, **122**, 11 678–11 702, https://doi.org/10.1002/2017JD027031.

Miller, M. A., and S. E. Yuter, 2013: Detection and characterization of heavy drizzle cells within subtropical marine stratocumulus using AMSR-E 89-GHz passive microwave measurements. *Atmos. Meas. Tech.*, **6**, 1–13, https://doi.org/10.5194/amt-6-1-2013.

Mitrescu, C., T. L'Ecuyer, J. Haynes, S. Miller, and J. Turk, 2010: *CloudSat* precipitation profiling algorithm: Model description. *J. Appl. Meteor. Climatol.*, **49**, 991–1003, https://doi.org/10.1175/2009JAMC2181.1.

Muhlbauer, A., I. L. McCoy, and R. Wood, 2014: Climatology of stratocumulus cloud morphologies: Microphysical properties and radiative effects. *Atmos. Chem. Phys.*, **14**, 6695–6716, https://doi.org/10.5194/acp-14-6695-2014.

Norris, J. R., 1998: Low cloud type over the ocean from surface observations. Part I: Relationship to surface meteorology and the vertical distribution of temperature and moisture. *J. Climate*, **11**, 369–382, https://doi.org/10.1175/1520-0442(1998)011<0369:LCTOTO>2.0.CO;2.

Oreopoulos, L., 2005: The impact of subsampling on MODIS level-3 statistics of cloud optical thickness and effective radius. *IEEE Trans. Geosci. Remote Sens.*, **43**, 366–373, https://doi.org/10.1109/TGRS.2004.841247.

Possner, A., R. Eastman, F. Bender, and F. Glassmeier, 2020: Deconvolution of boundary layer depth and aerosol constraints on cloud water path in subtropical stratocumulus decks. *Atmos. Chem. Phys.*, **20**, 3609–3621, https://doi.org/10.5194/acp-20-3609-2020.

Qu, X., A. Hall, S. A. Klein, and A. M. DeAngelis, 2015: Positive tropical marine low-cloud cover feedback inferred from cloud-controlling factors. *Geophys. Res. Lett.*, **42**, 7767–7775, https://doi.org/10.1002/2015GL065627.

Rosenfeld, D., Y. J. Kaufman, and I. Koren, 2006: Switching cloud cover and dynamical regimes from open to closed Benard cells in response to the suppression of precipitation by aerosols. *Atmos. Chem. Phys.*, **6**, 2503–2511, https://doi.org/10.5194/acp-6-2503-2006.

Savic-Jovcic, V., and B. Stevens, 2008: The structure and mesoscale organization of precipitating stratocumulus. *J. Atmos. Sci.*, **65**, 1587–1605, https://doi.org/10.1175/2007JAS2456.1.

Scott, R. C., T. A. Myers, J. R. Norris, M. D. Zelinka, S. A. Klein, M. Sun, and D. R. Doelling, 2020: Observed sensitivity of low-cloud radiative effects to meteorological perturbations over the global oceans. *J. Climate*, **33**, 7717–7734, https://doi.org/10.1175/JCLI-D-19-1028.1.

Stevens, B., and Coauthors, 2020: Sugar, gravel, fish and flowers: Mesoscale cloud patterns in the trade winds. *Quart. J. Roy. Meteor. Soc.*, **146**, 141–152, https://doi.org/10.1002/qj.3662.

Terai, C. R., and R. Wood, 2013: Aircraft observations of cold pools under marine stratocumulus. *Atmos. Chem. Phys.*, **13**, 9899–9914, https://doi.org/10.5194/acp-13-9899-2013.

Vaughan, M., S. Young, D. Winker, K. Powell, A. Omar, Z. Liu, Y. Hu, and C. Hostetler, 2004: Fully automated analysis of space-based lidar data: An overview of the *CALIPSO* retrieval algorithms and data products. *Proc. SPIE*, **5575**, 16–30, https://doi.org/10.1117/12.572024.

Wang, H., and G. Feingold, 2009: Modeling mesoscale cellular structure and drizzle in marine stratocumulus. Part I: Impact of drizzle on the formation and evolution of open cells. *J. Atmos. Sci.*, **66**, 3237–3256, https://doi.org/10.1175/2009JAS3022.1.

Watson-Parris, D., S. A. Sutherland, M. W. Christensen, R. Eastman, and P. Stier, 2021: A large-scale analysis of pockets of open cells and their radiative impact. *Geophys. Res. Lett.*, **48**, e2020GL092213, https://doi.org/10.1029/2020GL092213.

Wentz, F. J., and T. Meissner, 2004: AMSR-E/*Aqua* L2B global swath ocean products derived from Wentz algorithm, version 2 (L3 LWP). NSIDC, accessed 15 January 2020, https://nsidc.org/data/AE_Ocean/versions/2.

——, ——, C. Gentemann, and M. Brewer, 2014: Remote Sensing Systems *Aqua* AMSR-E (daily) environmental suite on 0.25 deg grid, version 7.0. Remote Sensing Systems, accessed 15 January 2020, http://www.remss.com/missions/amsr.

Wood, R., 2012: Stratocumulus clouds. *Mon. Wea. Rev.*, **140**, 2373–2423, https://doi.org/10.1175/MWR-D-11-00121.1.

——, and C. S. Bretherton, 2004: Boundary layer depth, entrainment, and decoupling in the cloud-capped subtropical and tropical marine boundary layer. *J. Climate*, **17**, 3576–3588, https://doi.org/10.1175/1520-0442(2004)017<3576:BLDEAD>2.0.CO;2.

——, and D. L. Hartmann, 2006: Spatial variability of liquid water path in marine low cloud: The importance of mesoscale cellular convection. *J. Climate*, **19**, 1748–1764, https://doi.org/10.1175/JCLI3702.1.

——, K. K. Comstock, C. S. Bretherton, C. Cornish, J. Tomlinson, D. R. Collins, and C. Fairall, 2008: Open cellular structure in marine stratocumulus sheets. *J. Geophys. Res.*, **113**, D12207, https://doi.org/10.1029/2007JD009371.

——, and Coauthors, 2018: Ultraclean layers and optically thin clouds in the stratocumulus-to-cumulus transition. Part I: Observations. *J. Atmos. Sci.*, **75**, 1631–1652, https://doi.org/10.1175/JAS-D-17-0213.1.

Yuan, T., H. Song, R. Wood, J. Mohrmann, K. Meyer, L. Oreopoulos, and S. Platnick, 2020: Applying deep learning to NASA MODIS data to create a community record of marine low cloud mesoscale morphology. *Atmos. Meas. Tech.*, **13**, 6989–6997, https://doi.org/10.5194/amt-13-6989-2020.